

A Rapid Reconstruction Method of Gamma Radiation Field based on Normalized Proper Orthogonal Decomposition

Kai Tan¹, Hojoon Son¹, Fan Zhang^{1*}

¹ Georgia Institute of Technology, North Avenue, Atlanta, GA 30332

- * Corresponding authors: fan.zhang@mc.gatech.edu

Abstract: When a fault occurs in nuclear facilities, accurately reconstructing gamma radiation fields through measurements from the mobile radiation detection (MRD) system becomes crucial to enable access to internal facility areas for essential safety assessments and repairs. Reconstruction of these fields is difficult because of the uncertainty in the positions and intensities of the gamma sources, the complexity of the gamma distribution, and the physics and radiation hardness constraints on the MRD systems. In this work, a novel reconstruction framework of the gamma radiation is proposed. This system entails a NPOD-based reconstruction algorithm with MRD data, and a variation-based adaptive measurements selection mechanism. Our approach has been thoroughly assessed using extensive simulations, and the results clearly prove its success and efficiency in reconstruction radiation fields accurately and quickly. Furthermore, the designed selection algorithm is also promising for extensive application to other optimization tasks of location selection.

Keywords: Radiation field reconstruction, Mobile radiation detection (MRD); Normalized proper orthogonal decomposition (NPOD), Variance-based adaptive selection

1 Introduction

The management of radiation radioactive materials within nuclear facilities is vital not only for the facility operational safety but also minimization of the environmental and health impacts¹⁻⁷. Periodically monitoring the distribution of gamma rays within the facility where radiation is potentially present is one of the important aspects of radiation safety management^{6, 8, 9}. This is crucial for two reasons: 1) maintaining an updated map of radiation distribution within the facility is essential for operational safety and regulatory compliance; 2) in the event of a radiation release or other emergencies, the radiation field can provide important information for emergency response units for fast and effective decisions that can minimize health risks and environmental consequences. Mobile radiation detection (MRD) systems are capable of accurately measuring radiation distributions and it is better than those fixed detection systems. MRD can monitor locations that the fixed detection system cannot cover and measure data in non-controlled and hazardous environments¹⁰. Specifically, in the cases of radiological/nuclear accidents, MRDs are able to deal with inherent uncertainties present in the physical environment¹⁰. Additionally, low-cost mobile radiation sensors attached to Unmanned Ground Vehicles (UGV), Unmanned Aerial Vehicles (UAV), or robots can reduce the total radiation monitoring cost^{11, 12}. However, MRD is capable of accurately measuring radiation distributions only when they are applied at very close intervals and taking these measurements

requires a large amount of measurement equipment which is time consuming¹³. Therefore, reconstructing a gamma radiation field using sparsely spaced measurements can significantly reduce costs and improve the applicability of MRD-based methods.

Reconstructing a gamma radiation field with sparse data, particularly post-incident within a nuclear facility, presents several challenges. First, the lack of precise information about the radiation source, such as its location and intensity, impedes the use of forward modelling techniques that rely on known parameters to reconstruct radiation field. This uncertainty often results in unreliable reconstruction outcomes. Second, the radiation map is highly nonlinear because shielding materials, such as wall or other nuclear materials, absorb and deflect gamma rays which will complicate the prediction of radiation spread and significantly increasing the complexity of the reconstruction task. Finally, MRD systems are limited in where they can safely navigate and collect data, resulting in sparse and potentially non-representative sampling of the radiation field. Therefore, these challenges demand innovative solutions and methodologies for accurate and efficient gamma radiation field reconstruction. Currently, a variety of methodologies are employed to reconstruct gamma radiation fields. Among these reconstruction methods, forward algorithms such as the Monte Carlo method^{14, 15} and the point kernel method^{16, 17} simulate potential radiation scenarios based on known source configuration. Conversely, inverse algorithms, such as the interpolation and model estimation methods, are designed to deal with scenario with unknown source configuration which is a common scenario in post-incident analyses or in environments where source distribution changes unpredictably and it is also the scenario that we will address in this work. The interpolation and model estimation methods are widely applied in multiple fields. In the field of meteorology, the ensemble kalman filter (EnKF) is used to enhances weather forecasting by dynamically integrating forecast models with observational data¹⁸. In oceanography, singular value decomposition (SVD) can perform well in reconstructing surface temperatures and currents from satellite and buoy data, which is crucial for enhancing marine navigation and facilitating climate research¹⁹. In medical imaging, specifically in MRI and CT scans, iterative reconstruction algorithms are utilized to improve the image quality by reducing noise and radiation exposure²⁰. In seismology, back-projection methods are essential for improving seismic hazard assessments by reconstructing the propagation of seismic waves²¹. Lastly, in radio astronomy, the CLEAN algorithm is employed to reconstruct images of celestial bodies, allowing scientists to resolve fine details of astronomical objects²².

Interpolation techniques such as Kriging have also proven valuable in nuclear engineering where they can be used to extrapolate existing data points and predict radiation levels in unmeasured areas²³. Zhou et al. improved the interpolation process using neural networks and achieved higher accuracy in radiation pattern prediction²⁴. Khuwaileh and West et al. used Gaussian process regression techniques to accurately map radiation fields with fewer measurements^{25, 26}. Zhu et al. introduced a modified Cahn-Hilliard equation to reconstruct the three-dimensional gamma dose rate around a nuclear waste container, taking into account the coupling effects of multiple sources of radioactive materials and complex environmental conditions^{27, 28}. Tan and Zhang used orthogonal basis decomposition (POD) technology to dynamically reconstruct nuclear power distribution and combined it with reinforcement learning methods to determine the optimal measurement points²⁹. These methods have many advantages, such as good processing capabilities in the case of sparse or incomplete data and the ability to produce high-resolution or physically consistent reconstruction results. However, they generally rely on computationally intensive and time-consuming processing. In disaster response or robot detection in unknown environments, where rapid reconstruction is required, the development of high-performance radiation field reconstruction systems faces great challenges, mainly due to the highly nonlinear characteristics of gamma radiation field distribution. This paper develops a novel method for reconstructing the gamma radiation field using Normalized Proper Orthogonal Decomposition (NPOD) with limited observations. In addition, a novel adaptive selection algorithm is proposed to find the best measurement locations for this system. This combined method enables rapid estimation of the gamma field distribution, to the point where it is feasible for a robotic system to mount sensors and estimate the field distribution in real-time. The proposed method is also applicable to general radioactive environments. Section 2 introduces detailed methods to reconstruct the gamma radiation fields regarding several measurements' locations. Section 3 presents the gamma reconstruction results in a complex radiation environment. Section 4 describes the summary and conclusion of this research.

2 Methodology

NPOD is utilized as a core reconstruction technique in the developed method. The NPOD method, an advanced form of the traditional Proper Orthogonal Decomposition (POD), is specifically designed to mitigate the bias introduced by unequal variance across different measurement dimensions and enhance the fairness and accuracy of the reconstructions. Besides,

an adaptive selection algorithm is proposed to optimize measurement locations, thereby significantly improving the reconstruction's accuracy and reliability

2.1 Proper Orthogonal Decomposition

The primary concept underlying POD, originally formulated in fluid dynamics to analyze turbulence, aims to optimally represent the velocity field $v(x, t) \in \mathbf{H}(\Omega, \mathbf{T})$, where $\mathbf{T} \subset \mathbb{R}; t \in \mathbf{T}; x \in \Omega \subset \mathbb{R}^n, n = 1, 2, \dots$. The task involves finding a deterministic function ϕ in a Hilbert space \mathbf{H} by resolving the following maximization problem³⁰:

$$\max_{\phi \in \mathbf{H}} \frac{\langle (v, \phi)^2 \rangle}{(\phi, \phi)} = \frac{\langle (v, \Phi)^2 \rangle}{(\Phi, \Phi)} \quad (1)$$

In which, $\langle \cdot \rangle$ symbolizes a statistical average operator, while (\cdot, \cdot) signifies the inner product of \mathbf{H} and $\| \cdot \|_{\mathbf{H}}^2$ represents the associated norm. If \mathbf{H} equals to $\mathbf{L}^2(\Omega)$, the maximization of problem (1) results in addressing the subsequent eigenvalue problem:

$$\int_{\Omega} \mathcal{R}(x, x') \Phi(x') dx' = \lambda \Phi(x) \quad (2)$$

The Hilbert-Schmidt theorem assures that there exists a set of positive eigenvalues $\lambda_1 \geq \lambda_2 \geq \dots \geq \lambda_N \geq 0$ and a set of eigenmodes $\{\Phi_1, \Phi_2, \dots, \Phi_N\}$ which is a Hilbert basis for \mathbf{H} . Thus, v can be decomposed according to the eigenmodes as

$$v(x, t) = \sum_{i=1}^{\infty} a_i(t) \Phi_i(x) \quad (3)$$

where a_i are the temporal coefficients, and $(\Phi_i)_{i \geq 1}$ are named modes. If the given functions are discrete like the problem presented in this work, POD can be carried out as follows:

Supposing there are M spatial positions that the robots can navigate, x_1, x_2, \dots, x_M in one sample. N sets of gamma radiation field data are obtained, written as matrix \mathbf{F} .

$$\mathbf{F} = \begin{bmatrix} F_1(x_1) & F_2(x_1) & \cdots & F_N(x_1) \\ F_1(x_2) & F_2(x_2) & \cdots & F_N(x_2) \\ \vdots & \vdots & \ddots & \vdots \\ F_1(x_M) & F_2(x_M) & \cdots & F_N(x_M) \end{bmatrix} \quad (4)$$

The corresponding correlation-matrix can be defined as

$$\mathbf{C} = \frac{1}{M} \mathbf{F}^T \mathbf{F} \quad (5)$$

The eigenvalues $\lambda_1 \geq \lambda_2 \geq \dots \geq \lambda_N \geq 0$ and the corresponding eigenvectors, A_1, A_2, \dots, A_N , can be solved based on Eq. (6).

$$\mathbf{C}\mathbf{A} = \lambda\mathbf{A} \quad (6)$$

Then, matrix Φ can be calculated.

$$\Phi_{M \times N} = \mathbf{F} \cdot \mathbf{A} \quad (7)$$

Where $\mathbf{A} = [A_1, A_2, \dots, A_N]$. To make $\Phi_{M \times N}$ be orthonormal, its each column should be divided by $\sqrt{\lambda_i}, (i = 1, \dots, N)$, and the mode functions $\left[\frac{\Phi_1}{\sqrt{\lambda_1}}, \frac{\Phi_2}{\sqrt{\lambda_2}}, \dots, \frac{\Phi_N}{\sqrt{\lambda_N}} \right]$ can be obtained. Similarly, the POD coefficients are calculated.

$$a_i = \frac{1}{\sqrt{\lambda_i}} \mathbf{F} \Phi_i, i = 1, 2, 3 \dots N \quad (8)$$

Therefore, the gamma radiation field at any time which also referred to any condition, $\mathbf{F}(t)$, can be obtain by

$$\mathbf{F}_t(\mathbf{x}) = \begin{bmatrix} F_t(x_1) \\ F_t(x_2) \\ \vdots \\ F_t(x_m) \end{bmatrix} = \Phi_{M \times N} \cdot \begin{bmatrix} a_1(t) \\ a_2(t) \\ \vdots \\ a_N(t) \end{bmatrix} \quad (9)$$

If the first K orders are used, $\mathbf{F}_t(\mathbf{x})$ can also be formulated as:

$$\mathbf{F}_t(\mathbf{x}) = \Phi_{M \times K} \cdot \begin{bmatrix} a_1(t) \\ a_2(t) \\ \vdots \\ a_K(t) \end{bmatrix}, (K < N) \quad (10)$$

Generally, the reconstruction coefficients $a_i(t)$ can be derived from the measurements collected by MRD with the number of measurement locations surpassing K and then Least-Square Method (LSM) is employed to calculate the coefficients, which means the number of measurement location and their combinations highly influence on performance of reconstruction³⁰. When a POD based reconstruction system is deployed in the real world, it has no advance knowledge of how many discrete sources are present, how energetic each one might be, or what is the density of each source. Therefore, to equip the POD based reconstruction system with broad generalization, thousands of synthetic cases—randomly sampling the number of sources, their activities, and their positions across the domain—are generated. However, the variance of the radiation-intensity grows with the square of the net source strength (as demonstrated analytically in Appendix A), which will cause high-activity or multi-source scenarios possess far larger pointwise variances than those populated by weak or sparse configurations. To remedy this, Normalized POD (NPOD) is introduced. The key step is to standardize each row of \mathbf{F} by subtracting the mean and dividing by the standard deviation,

thereby equalizing variance contributions from all points. Concretely, let μ_i and σ_i be the mean and standard deviation of location x_i , and define the standardized matrix $\tilde{\mathbf{F}}$ by

$$\tilde{F}_j(x_i) = \frac{F_j(x_i) - \mu_i}{\sigma_i}, \quad 1 \leq i \leq M, \quad 1 \leq j \leq N \quad (11)$$

the corresponding normalized modes $\tilde{\Phi}$ is obtained by implementing the POD steps (Eqs. 5, 6, 7) on $\tilde{\mathbf{F}}$. Each location now exerts an equal influence on the decomposition due to a standardized $\tilde{\mathbf{F}}$, which will prevent high-intensity points from monopolizing the principal modes. Figure 2 shows the process of using the NPOD method for reconstructing a gamma radiation map. In this framework, the first step involves evenly dividing the original data into a training set and a test set. The training set is utilized to generate a NPOD model, and the measurements is normalized by mean $\mu(\mathbf{x})$ and standard deviation $\sigma(\mathbf{x})$ from the training data and then $a_i(t)$ is calculated. Finally, we revert to the original scale by following equation:

$$F_t(x_i) = \sigma_i \tilde{F}_t(x_i) + \mu_i \quad (12)$$

By balancing the variance of all input dimensions, NPOD preserves information about both strong and weak field features, significantly improving the reconstruction fidelity of low-intensity sources. Finally, the number of modes can be determined by the cumulative energy ratio, defined as³¹

$$E_k = \frac{\sum_{i=1}^k \tilde{\lambda}_i}{\sum_{i=1}^N \tilde{\lambda}_i} \quad (13)$$

Where $\tilde{\lambda}_i$ is eigenvalue of NPOD. We choose K such that E_K meets a desired threshold and ensures an appropriate balance between model complexity and accuracy.

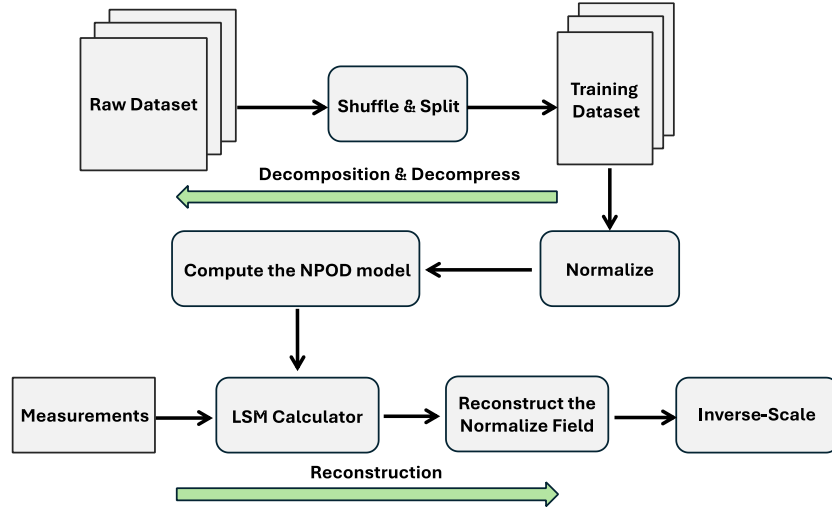


Figure 2 The flow of NPOD implement in the reconstruction problem.

2.2 An Adaptive Selection Algorithm of Measurement Points for NPOD based Reconstruction System

The combination of measurement locations has a significant impact on the performance of NPOD-based reconstruction systems. At the same time, environmental complexity, robot mobility limitations, and radiation dose limitations will limit the number and location of sampling points. Therefore, the selection of optimized measurement locations is crucial to achieve high reconstruction accuracy with as few samples as possible. For this combinational problem, advanced algorithms and techniques (e.g., genetic algorithms, particle swarm optimization, or simulated annealing) can be utilized to iteratively optimize the sampling locations. These methods account for the complex interactions between environmental features and radiation propagation, ensuring that the selected points provide the most useful data for reconstructing the radiation landscape. However, in the real world, the huge search space often makes it impossible for traditional optimization algorithms to find satisfactory solutions within limited computing resources. For example, consider modeling an environment that may contain 10,000 potential measurement grid points. Identifying the subset of 200 points requires testing a large number of combinations from these 10,000 points to ultimately find 200 viable combinations. Furthermore, evaluating the effectiveness of any chosen combination of positions for NPOD reconstruction on a test dataset is very time-consuming.

To overcome this obstacle, a reverse engineering strategy is adopted from the perspective of the factor that LSM minimizes discrepancies only at those sampled locations which can hardly make global accuracy to guarantee in complex fields³⁴. Algorithm 1 shows the concise flow of this adaptive selection method. It typically starts with an initial set \mathcal{S}_0

chosen randomly (without replacement) such that $m_0 = |\mathcal{S}_0| \geq L$ because the NPOD reconstruction coefficients cannot be calculated if the number of measurement points is smaller than L . Then, the NPOD coefficients are estimated at iteration n by LSM:

$$a^{(n)} = \arg \min_{a \in \mathbb{R}^L} \sum_{\mathbf{x} \in \mathcal{S}_n} \left(F(\mathbf{x}) - \sum_{\ell=1}^L a_\ell \phi_\ell(\mathbf{x}) \right)^2 \quad (14)$$

Where $F(\mathbf{x})$ is the true (but unknown) scalar field in the domain; $\mathcal{S}_n \subset \Omega$ is the set of measurement points at iteration n , with $m_n = |\mathcal{S}_n|$. The relative residuals is used to evaluate the current measurement set which is defined as:

$$e_n(\mathbf{x}) = \left| \frac{F(\mathbf{x}) - F^{(n)}(\mathbf{x})}{F(\mathbf{x})} \right| \quad (15)$$

Where $F^{(n)}(\mathbf{x}) = \sum_{\ell=1}^L a_\ell^{(n)} \phi_\ell(\mathbf{x})$ is the NPOD reconstruction at iteration n . The algorithm then locates the point \mathbf{x}_n^* with the largest absolute error:

$$\mathbf{x}_n^* = \arg \max_{\mathbf{x} \in \Omega} e_n(\mathbf{x}) \quad (16)$$

If this maximum error $\text{MaxE}(n)$ falls below the target MaxET which is the desired upper bound for the maximum absolute reconstruction error or if the change in maximum error between successive iterations is below δ , we conclude that the algorithm has reached the desired accuracy. Otherwise, we include \mathbf{x}_n^* in the measurement set for the next iteration, measure $F(\mathbf{x}_n^*)$, and solve the LSM problem again. In doing so, the algorithm iteratively refines the measurement set until either the maximum number of points N_p is reached or the reconstruction quality meets the requirement.

Algorithm 1: Adaptive Measurement Points Selection

1. Initialization: Randomly select an initial measurement set $\mathcal{S}_0 \subset \Omega$ of size $m_0 \geq L$.
2. For $n = 0, 1, 2, \dots$ while $m_n \leq N_p$
 - a) Update NPOD Coefficients: $a^{(n)}$
 - b) Compute Residuals: Calculate $e_n(\mathbf{x}) = F(\mathbf{x}) - F^{(n)}(\mathbf{x})$.
 - c) Find Maximum Error:

$$\text{MaxE}(n) = \max_{\mathbf{x} \in \Omega} |e_n(\mathbf{x})|, \mathbf{x}_n^* = \arg \max_{\mathbf{x} \in \Omega} |e_n(\mathbf{x})|.$$

- d) If $\text{MaxE}(n) \leq \text{MaxET}$ **or** If $n \geq 1$ and $|\text{MaxE}(n) - \text{MaxE}(n-1)| \leq \delta$
 - Add New Measurement:

$$\mathcal{S}_{n+1} = \mathcal{S}_n \cup \{\mathbf{x}_n^*\}; \text{measure } F(\mathbf{x}_n^*).$$

3 Output

- Final measurement set \mathcal{S}_* (with $|\mathcal{S}_*| \leq N_p$)
- NPOD coefficient vector $\mathbf{a}^{(*)} = [a_1^{(*)}, \dots, a_L^{(*)}]^\top$

By iteratively adding the point with the largest error, this "greedy" procedure rectifies the most serious deficiency at each step and improves the overall NPOD reconstruction. Unlike a global combinatorial optimization, the adaptive selection algorithm offers a practical solution that converges quickly while reducing the maximum reconstruction error throughout the domain. This efficiency is due to the synergistic effect of NPOD modes, which capture the dominant patterns of the field, and the error-driven placement, which focuses new data on the regions where the current model is most uncertain.

2.4 Genetic Algorithms

Genetic Algorithm (GA) draws on the natural selection and inheritance mechanism of the biological world and can efficiently explore and find approximate optimal solutions in complex high-dimensional search spaces³⁵. Due to its good adaptability to nonlinear constraint problems, GA is often used as a benchmark for evaluating new optimization methods. Algorithm 2 shows the basic process of GA for screening the optimal measurement point configuration: first, a set of candidate solutions is randomly generated as the initial population, and each candidate solution can be regarded as a chromosome containing several "genes"; then, in each generation, the population performance is evaluated through the fitness function, and excellent individuals are selected for crossover and mutation to reproduce the next generation. The performance of the algorithm is mainly controlled by the following hyperparameters: the population size, N_{pop} , determines the number of candidate solutions for parallel search. The larger the population size, the richer the genetic diversity, which helps to escape the local optimum; The mutation rate, MuR , randomly changes some genes in the solutions, ensuring that the algorithm does not get stuck in local optima. Meanwhile, the maximum number of generations, max_gen , controls when the GA stops, striking a balance between thorough exploration and computational feasibility. The elite percentage, Ep , helps preserve quality solutions by passing a fixed percentage of top-performing individuals unchanged into the next generation.

Algorithm 2: Genetic Algorithms

1. Input: N_{pop} , MuR , max_gen , NPOD model with certain number of models, Ep
2. Initialize population with N_{pop} individuals, each individual is a binary vector representing positions.
3. Initialize generation counter, $g = 1$
4. **While** $g \leq max_gen$ **do**
 - Compute fitness of each individual in the population based on the reconstruction results with NPOD.
 - Sort individuals based on fitness and select Ep of the population as elites.
 - Perform roulette wheel selection to fill the new generation.
 - Apply crossover and mutation operations to create new individuals until the population reaches N_{pop}
 - Replace the least fit individuals with elites to maintain Ep
 - Update population with new generation. $g = g + 1$
5. Select the best individual based on fitness after all generations.
6. Decode the best individual to determine the optimal measurement positions.
7. Return the best individual .eg. the optimal measurement positions.

3 Results

In this study, a framework for gamma radiation field reconstruction based on the NPOD is developed, as shown in Figure 2. This framework comprises two primary components: 1) the construction of the NPOD model, and 2) the determination of an optimal configuration for measurement locations based on adaptive selection algorithm. In terms of robustness, the dataset is expanded to encompass a wide variety of real-world conditions within the gamma radiation environment. This approach ensures that the NPOD-based framework is equipped to deliver high performance across diverse scenarios, including fields generated by various numbers and configurations of radiation sources.

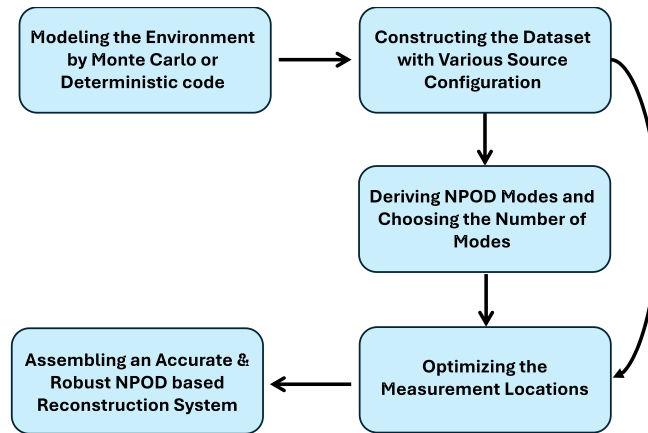


Figure 2 NPOD based gamma radiation field reconstruction framework.

3.1 NPOD mode calculation

To validate the effectiveness and resilience of our proposed method, we introduce a testing scenario more complex than what is typically encountered in nuclear facilities. This scenario involves a dense array of obstacles and a complicated configuration of radiation sources, resulting in a complex pattern of gamma radiation distribution. The scenario's testing ground covers an area of 96 meters by 72 meters, as detailed in Figure 3 and Table 1. It mimics a realistic setting with air-filled spaces and concrete walls, mirroring common materials found in nuclear facilities. Through addressing the complexities of this scenario, our method aims to prove its practicality for real-world scenarios, particularly in contexts where understanding and minimizing gamma radiation's impact is essential. To enhance the robustness of our framework, we employ a strategy for selecting various configurations of radiation sources. This involves first deciding on the number of sources, followed by placing these sources randomly within a designated source area (highlighted in red). We examined configurations with 1, 2, 4, 6, 10, 15, 20, 40, 60, 100 sources and 450 cases for each source configuration. In total, 4500 distinct scenarios were created for analysis, each with a specific number of sources. The simulation of gamma radiation distribution across these scenarios was conducted using OpenMC³⁶, with a spatial resolution of 100x100 mesh points for each scenario.

Table 1 The parameters of geometry used in testing case.

Parameters Objectives	Location (x, y)	Height (m)	Width (m)
Wall 1	(-23.5, 8.5)	3.0	1.0
Wall 2	(-18.5, -10.5)	1.0	3.0
Wall 3	(2.5, -14.5)	1.0	3.0
Wall 4	(18.5, 3.5)	3.0	1.0
Wall 5	(6.5, 20.5)	1.0	3.0
Wall 6	(-10.5, 24.5)	1.0	3.0
Source region	(0, 0)	4.0	4.0

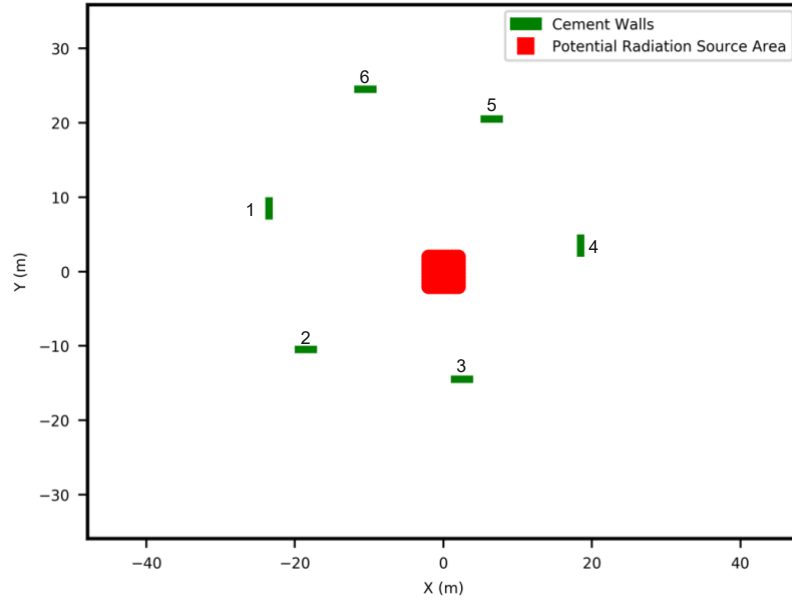


Figure 3 The geometry of testing case

Figure 4 presents the cumulative energy distribution of NPOD modes, illustrating how the cumulative energy ratio E_k evolves as the number of modes increases. Notably, the value of E_k approaches nearly 1 indicating almost complete representation of the system's energy when the number of modes reaches 70. Beyond this point, any increase in the number of modes results in only marginal changes in the cumulative energy ratio. Based on this observation, the decision to select 70 as the optimal number of modes for the NPOD model in this work is justified.

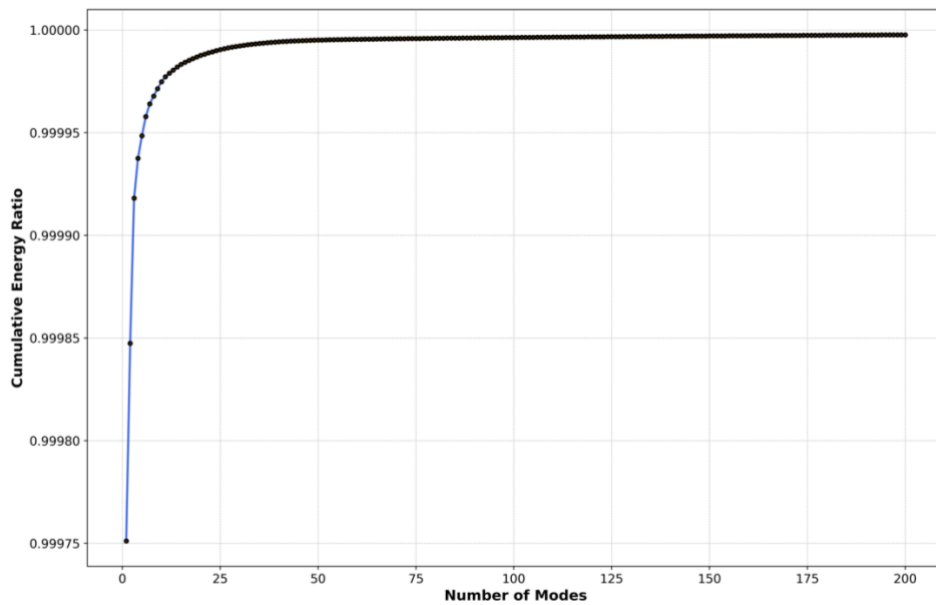


Figure 4 The cumulative energy distribution of NPOD modes

3.2 Optimization of Measurement Location and Reconstruction Results

In this study, the Absolute Relative Error (ARE), Mean Absolute Relative Error (MARE), and the Maximum Absolute Relative Error (MaxARE) are utilized as the evaluation metrics for assessing the efficacy of our framework. These metrics are defined as

$$ARE_i = \left| \frac{\mathbf{F}_i^{pre} - \mathbf{F}_i}{\mathbf{F}_i} \right| \quad (14)$$

$$MARE = \frac{1}{N} \sum_{i=1}^N ARE_i \quad (15)$$

$$MaxARE = \text{Max}\{ARE_i, i = 1, 2, 3 \dots N\} \quad (16)$$

In which N is the number of test cases, \mathbf{F}_i is the reference for all the location node the robot can navigate, calculated by OpenMC, and \mathbf{F}_i^{pre} is reconstruction results for i -th case. The dataset was randomly split into a training subset (75 %) and a test subset (25 %) and 70 NPOD modes were then constructed from the training subset. To assess reconstruction performance on the entire dataset, 160 measurement points were drawn at random from 9965 potential locations, and the previously derived NPOD modes were applied. Hence, the outcomes presented in Figures 5 and 6 reflect this complete workflow—mode construction on the training data followed by reconstruction of the full dataset using the selected measurement points. Analysis of the reconstruction metrics (Figures 5 and 6) shows that the MARE remains below 1.8 % for the vast majority of test cases, while instances in which the MaxARE exceeds 20 % are scarce. Under the current measurement-point configuration and NPOD-mode allocation, reconstruction errors are therefore well constrained, with only isolated cases exhibiting elevated discrepancies. Nonetheless, Figure 6 also reveals a small number of outlier cases in which MaxARE surpasses 200 %, a magnitude that is untenable for safety-critical applications. Accordingly, subsequent sensor-layout optimization should place primary emphasis on suppressing MaxARE, aiming to eliminate such extreme discrepancies while preserving the already low average error levels.

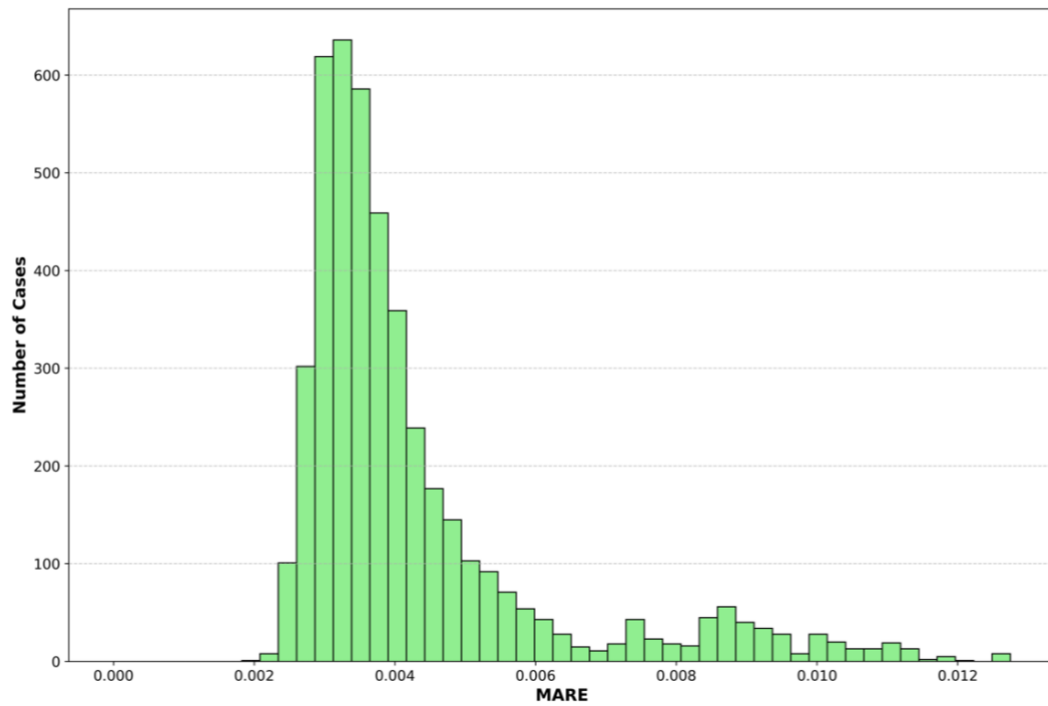


Figure 5 MARE distribution on test dataset with 70 NPOD modes and 160 randomly selected measurement points

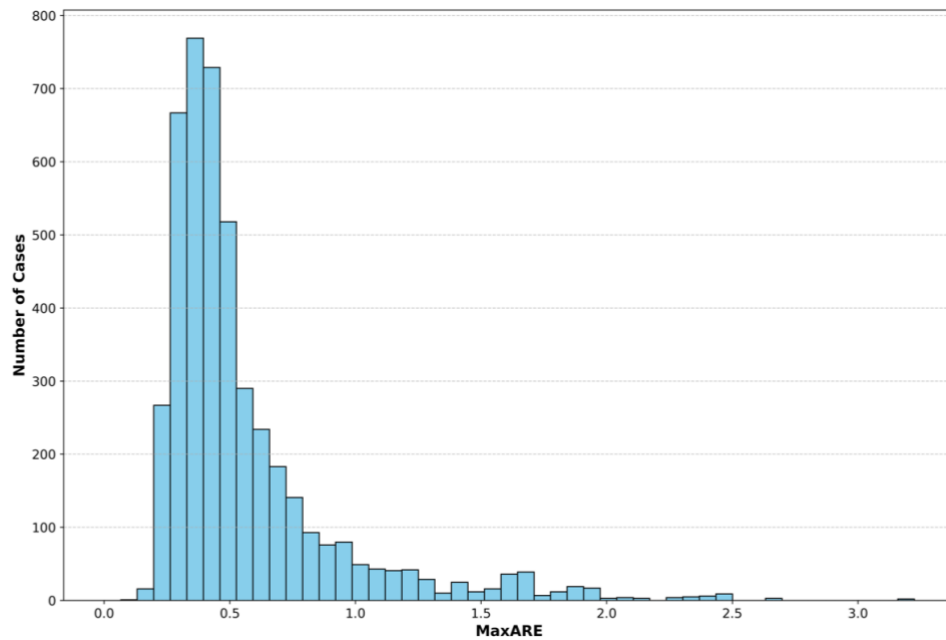


Figure 6 MaxARE distribution on test dataset with 70 NPOD modes and 160 randomly selected measurement points

The essence of the adaptive selection algorithm is to choose measurement points that contain as much informative content as possible while avoiding redundancy. From an information-

theoretic perspective, points exhibiting larger variance are deemed more valuable because they contribute more distinct information toward reconstructing the entire field³⁷⁻⁴⁰. Therefore, a variance based initialization measurement location method is proposed, and its first step is to rank the measurement variances in descending order, and the top 70 positions (matching the number of NPOD modes) are selected as the initial measurement set. Figure 7 compares random measurement-point layouts with the proposed variance based initialization scheme, demonstrating that selecting these strategically informative locations not only hastens algorithmic convergence but also improves reconstruction accuracy—yielding a notably smaller MaxARE. These findings underscore the advantage of targeting high-variance points as a more efficient route to comprehensive field reconstruction.

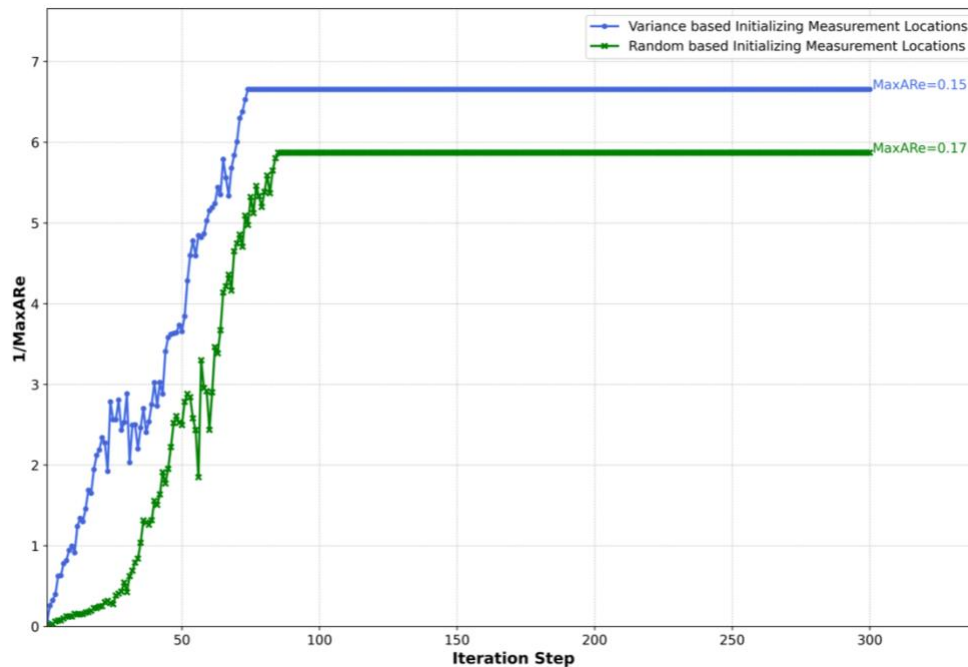


Figure 7 The comparison of random and variance-based measurement location initialization methods

Figure 8 shows the results of the traditional GA method. It is apparent that the GA method struggles to find the optimal values and converges more slowly than the developed method. This issue may stem from the vast search space (needing to find a combination of 160 superior positions out of 9948 possible ones to minimize error). It is worth noting that the choice of 160 positions is because the proposed optimization algorithm converged upon finding 160 positions. In other words, the additional precision would require increasing the NPOD modes. To fairly compare the advantages of the proposed method over traditional ones, the number of final measurement positions was standardized. Furthermore, to eliminate the influence of hyperparameter settings on the GA's performance, grid search was employed for

hyperparameter optimization. After considerable effort, a relatively good set of hyperparameters was identified as shown in Figure 8. Figures 9 and 10 compile the reconstruction accuracy achieved with the variance-based sensor-placement strategy. Figure 9 displays the distribution of MaxARE for each group of 150 test cases, while Figure 10 summarizes MARE over the same groups. Across the entire benchmark suite, MaxARE clusters tightly around 6 % and never exceeds 15 %, and every MARE lies below 1.6 %. Each individual test case contains predictions at 9948 spatial locations. Box-plot whiskers and outlier dispersions reveal that, on average, more than 60 % of those pointwise errors fall beneath an ARE of 1.5 %. Together, these statistics demonstrate that the proposed adaptive-placement framework delivers consistently high-fidelity reconstructions of complex gamma-radiation fields, validating both the measurement-location optimizer and the underlying NPOD-based inversion methodology.

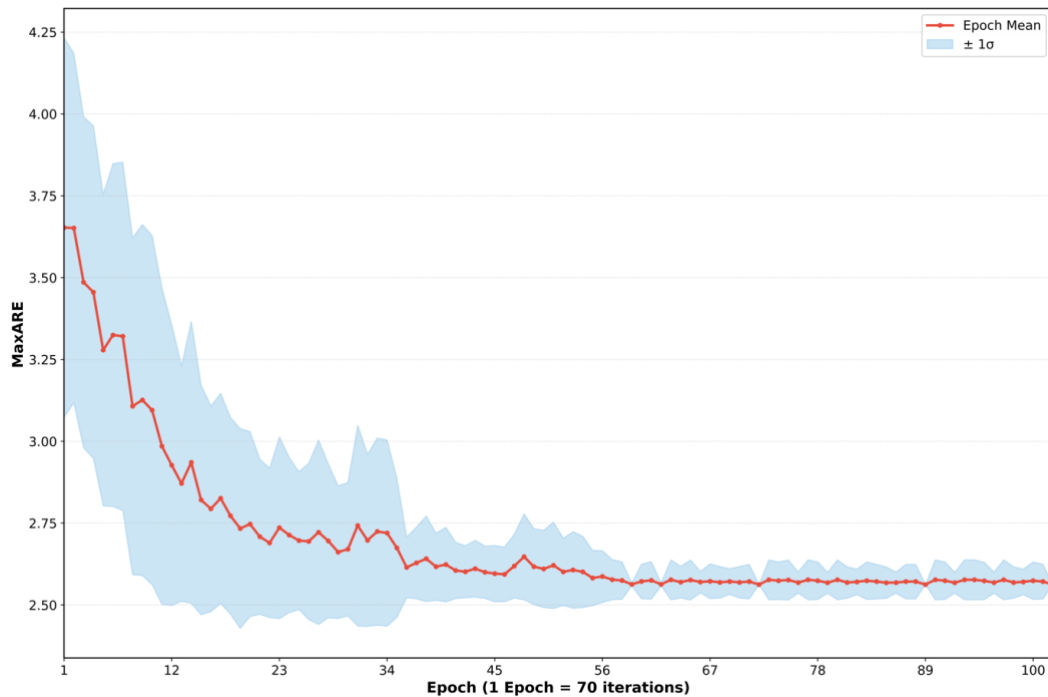


Figure 8 The performance of convergence with GA methods

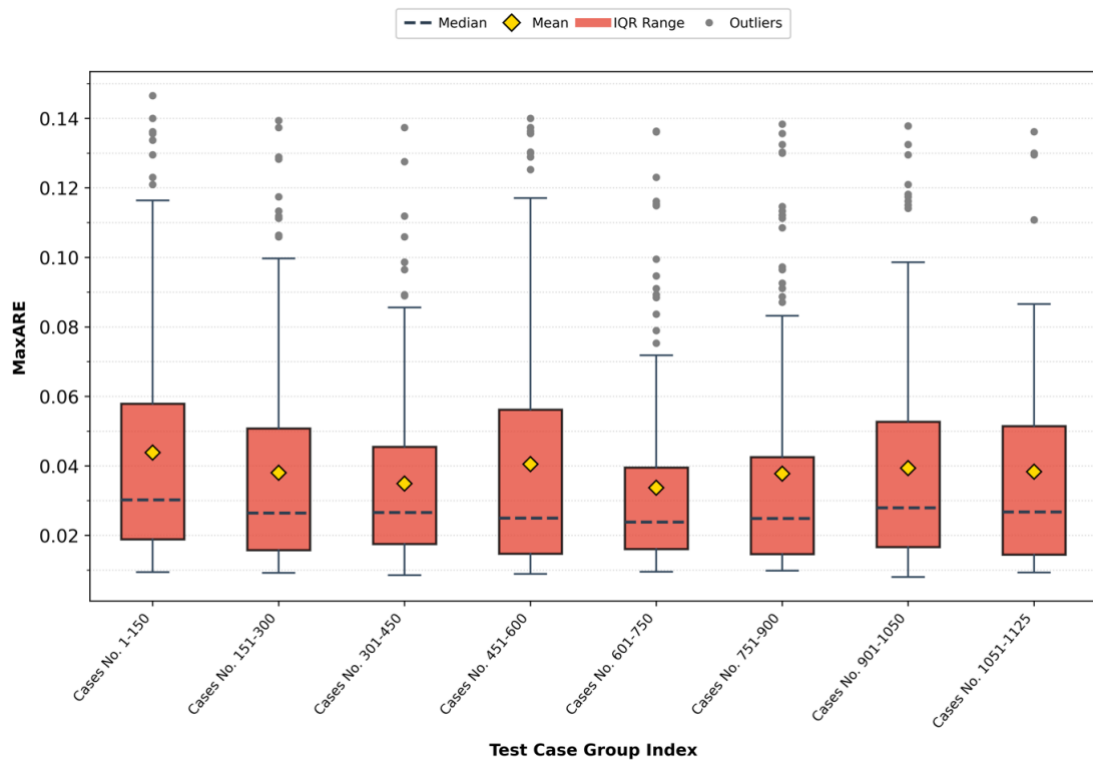


Figure 8 The distribution of MaxARE on test dataset

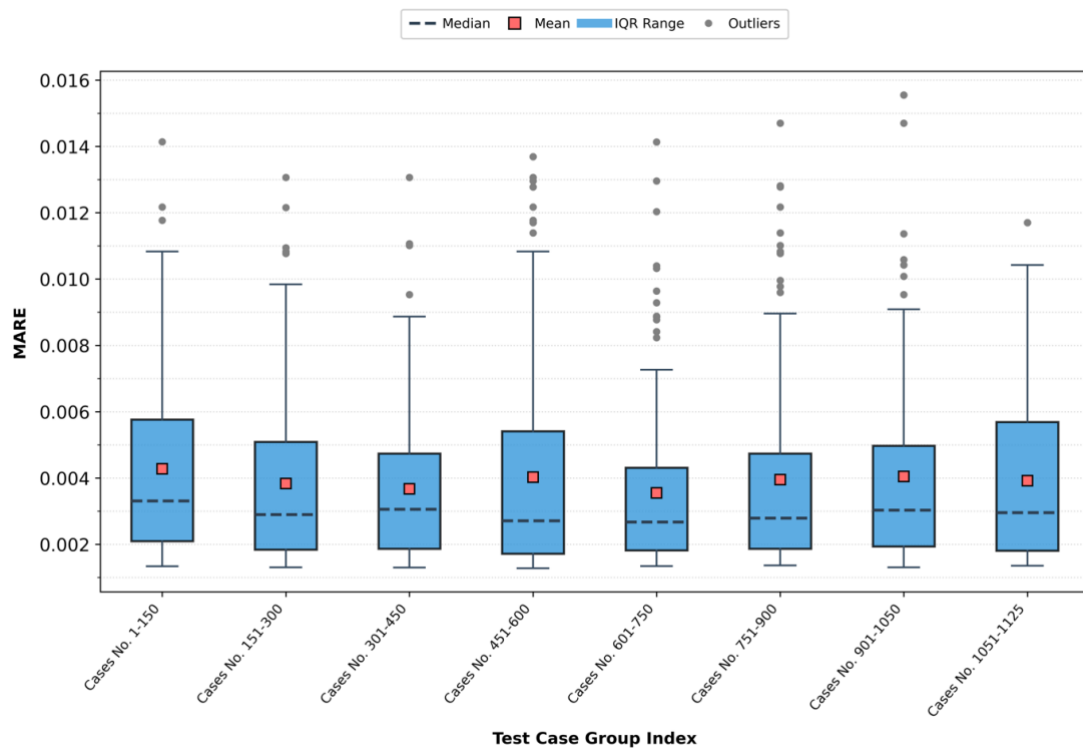


Figure 9 The distribution of MARE on test dataset

Notably, when using a computing setup with a 96-processor, 128GB RAM, and an AMD EPYC 7763 64-Core Processor to reconstruct 1125 test cases simultaneously, the process

took about 20 seconds in total. This equates to approximately 0.014 seconds per case, a speed that fully meets real-time requirements. This methodology leverages the informational richness inherent in locations with high variability to enhance field reconstruction. By selecting initial positions based on their variance, the optimization process is streamlined, leading to more accurate and faster convergence. The comparison with traditional GA methods, which struggle in the vast search space, underscores the efficiency of the proposed approach. The NPOD-based framework's capability to rapidly process numerous test cases with high accuracy highlights its potential for practical applications, especially in scenarios requiring quick and reliable field reconstructions.

4 Conclusion

This paper introduces a novel framework for reconstructing gamma radiation fields, integrating NPOD with an advanced variance-based adaptive selection algorithm, which is distinguished by its computational efficiency and accuracy. Our quantitative evaluations reveal that the framework consistently achieves minimal error rates in radiation field reconstruction, with ARE around 6%, never exceeding 15%, and maintaining a MARE below 1.6% across various test scenarios, underscoring its reliability. Additionally, our proposed adaptive selection algorithm significantly outperforms traditional methods such as Genetic Algorithms, excelling in convergence speed and error minimization and demonstrating potential for broader application in optimizing measurement configurations in various optimization tasks. The framework's robustness was rigorously tested in simulated environments that closely replicate real-world conditions, encompassing a comprehensive evaluation set of 4500 distinct scenarios. By combining precise measurement location optimization with sophisticated computational techniques, our NPOD-based reconstruction framework and its accompanying adaptive measurement selection algorithm enable faster and more accurate radiation field reconstruction, enabling substantial improvements in nuclear facility management and emergency response strategies. The current POD model considers only single-energy gamma radiation, which may limit accuracy in practical settings where energy spectra vary (especially in dose-focused applications). In addition, the present measurement point selection strategy does not yet account for the risks or movement constraints of mobile detector platforms (such as robots operating in hazardous environments). Future work should extend the framework to handle multi-energy gamma radiation modelling to improve realism and accuracy in dose estimation, and incorporate platform risks, mobility constraints, and operational safety considerations into the measurement optimization process, with the ultimate goal of developing a more accurate

and practical reconstruction system suitable for real-world applications such as nuclear facility monitoring and emergency response.

Reference

- [1]M. Y. H. Bangash, *Structures for Nuclear Facilities: Analysis, Design, and Construction*. Berlin, Germany: Springer, 2011.
- [2]*Site Evaluation of Nuclear Facilities*, Safety Code AERB/NF/SC/S (Rev-1), Atomic Energy Regulatory Board, Mumbai, India, 2014.
- [3]F. El Ghissassi *et al.*, “A review of human carcinogens—Part D: radiation,” *Lancet Oncol.*, vol. 10, no. 8, pp. 751–752, Aug. 2009.
- [4]A. J. González, “Radiation safety standards and their application: international policies and current issues,” *Health Phys.*, vol. 87, no. 3, pp. 258–272, 2004.
- [5]C. R. Harrell *et al.*, “Risks of using sterilization by gamma radiation: the other side of the coin,” *Int. J. Med. Sci.*, vol. 15, no. 3, pp. 274–282, 2018.
- [6]*Radiation Protection and Safety of Radiation Sources: International Basic Safety Standards*, Interim ed., International Atomic Energy Agency, Vienna, Austria, 2011.
- [7]K. Prasad, W. Cole, and G. Haase, “Radiation protection in humans: extending the concept of ALARA from dose to biological damage,” *Br. J. Radiol.*, vol. 77, no. 914, pp. 97–99, 2004.
- [8]B. Pomaro, “A review on radiation damage in concrete for nuclear facilities: from experiments to modeling,” *Model. Simul. Eng.*, vol. 2016, Art. no. 9459013, 2016.
- [9]S. Moontaha *et al.*, “Real-time environmental gamma-radiation dose-rate measurement around major nuclear and radiological facilities in Bangladesh,” *Int. J. Sci. Res. Manag.*, vol. 6, no. 3, pp. 57–63, 2018.
- [10]L. Marques, A. Vale, and P. Vaz, “State-of-the-art mobile radiation detection systems for different scenarios,” *Sensors*, vol. 21, no. 4, Art. no. 1051, Feb. 2021.
- [11]N. A. A. Rahman *et al.*, “A coverage path-planning approach for autonomous radiation mapping with a mobile robot,” *Int. J. Adv. Robot. Syst.*, vol. 19, no. 4, Art. no. 17298806221116483, 2022.
- [12]Š. Čerba *et al.*, “Unmanned radiation-monitoring system,” *IEEE Trans. Nucl. Sci.*, vol. 67, no. 4, pp. 636–643, Apr. 2020.
- [13]J. Paridaens, “Development of a low-cost GPS-based upgrade to a standard handheld gamma detector for mapping environmental radioactive contamination,” *Appl. Radiat. Isot.*, vol. 64, no. 2, pp. 264–271, 2006.
- [14]D. Mackin *et al.*, “Evaluation of a stochastic reconstruction algorithm for use in Compton-camera imaging and beam-range verification from secondary gamma emission during proton therapy,” *Phys. Med. Biol.*, vol. 57, no. 11, pp. 3537–3553, 2012.
- [15]T. Kawano *et al.*, “Monte Carlo simulation for particle and γ -ray emissions in the statistical Hauser–Feshbach model,” *J. Nucl. Sci. Technol.*, vol. 47, no. 5, pp. 462–469, 2010.
- [16]M. Prokhorets *et al.*, “Point-kernel method for radiation-fields simulation,” *Vopr. At. Nauki Tekh.*, ser. Nuclear Physics Investigations, no. 4, pp. 118–122, 2007.
- [17]G. Wang and J. Qi, “PET image reconstruction using kernel method,” *IEEE Trans. Med. Imaging*, vol. 34, no. 1, pp. 61–71, Jan. 2015.
- [18]G. Evensen, “The ensemble Kalman filter: Theoretical formulation and practical implementation,” *Ocean Dyn.*, vol. 53, pp. 343–367, 2003.

- [19]J. M. Wallace, C. Smith, and C. S. Bretherton, "Singular value decomposition of wintertime sea-surface-temperature and 500-mb-height anomalies," *J. Climate*, vol. 5, no. 6, pp. 561–576, 1992.
- [20]J. A. Fessler, "Statistical image-reconstruction methods for transmission tomography," in *Handbook of Medical Imaging*, M. Sonka and J. M. Fitzpatrick, Eds. Bellingham, WA, USA: SPIE, 2000, vol. 2, pp. 1–70.
- [21]Y. Xu *et al.*, "Rupture imaging of the Mw 7.9 12 May 2008 Wenchuan earthquake from back-projection of teleseismic P waves," *Geochem. Geophys. Geosyst.*, vol. 10, no. 4, Art. no. Q04006, 2009.
- [22]J. Högbom, "Aperture synthesis with a non-regular distribution of interferometer baselines," *Astron. Astrophys. Suppl.*, vol. 15, pp. 417–426, 1974.
- [23]Y. Sanada and T. Torii, "Aerial radiation monitoring around the Fukushima Dai-ichi nuclear power plant using an unmanned helicopter," *J. Environ. Radioact.*, vol. 139, pp. 294–299, 2015.
- [24]W. Zhou *et al.*, "BP neural-network-based reconstruction method for radiation-field applications," *Nucl. Eng. Des.*, vol. 380, Art. no. 111228, 2021.
- [25]B. A. Khuwaileh and W. A. Metwally, "Gaussian-process approach for dose mapping in radiation fields," *Nucl. Eng. Technol.*, vol. 52, no. 8, pp. 1807–1816, 2020.
- [26]A. West *et al.*, "Use of Gaussian-process regression for radiation mapping of a nuclear reactor with a mobile robot," *Sci. Rep.*, vol. 11, Art. no. 13975, 2021.
- [27]S. Zhu *et al.*, "3-D gamma-radiation-field reconstruction using limited measurements for multiple radioactive sources," *Ann. Nucl. Energy*, vol. 175, Art. no. 109247, 2022.
- [28]S. Zhu *et al.*, "3-D gamma dose-rate reconstruction for a radioactive-waste-processing facility using sparse and arbitrarily positioned measurements," *Prog. Nucl. Energy*, vol. 144, Art. no. 104073, 2022.
- [29]K. Tan and F. Zhang, "Optimizing the fixed-number detector placement for the nuclear-reactor core using reinforcement learning," *Nucl. Sci. Eng.*, early access, pp. 1–23, 2024.
- [30]J. Weiss, "A tutorial on the proper orthogonal decomposition," in *Proc. AIAA Aviation Forum*, Dallas, TX, USA, 2019, Paper 3333.
- [31]H. Chen *et al.*, "A practical guide for using proper orthogonal decomposition in engine research," *Int. J. Engine Res.*, vol. 14, no. 4, pp. 307–319, 2013.
- [32]D. Ruan *et al.*, "Normalized proper orthogonal decomposition for building-pressure data compression," *J. Wind Eng. Ind. Aerodyn.*, vol. 94, no. 6, pp. 447–461, 2006.
- [33]S. Kho, C. Baker, and R. Hoxey, "POD/ARMA reconstruction of the surface-pressure field around a low-rise structure," *J. Wind Eng. Ind. Aerodyn.*, vol. 90, no. 12–15, pp. 1831–1842, 2002.
- [34]Å. Björck, "Least-squares methods," in *Handbook of Numerical Analysis*, P. Ciarlet and J.-L. Lions, Eds. Amsterdam, The Netherlands: North-Holland, 1990, vol. 1, pp. 465–652.
- [35]J. H. Holland, "Genetic algorithms," *Sci. Am.*, vol. 267, no. 1, pp. 66–73, Jul. 1992.
- [36]P. K. Romano *et al.*, "OpenMC: A state-of-the-art Monte Carlo code for research and development," *Ann. Nucl. Energy*, vol. 82, pp. 90–97, 2015.
- [37]D. Y. Oh and H. C. No, "Determination of the minimal number and optimal sensor location in a nuclear system with fixed incore detectors," *Nucl. Eng. Des.*, vol. 152, no. 1–3, pp. 197–212, 1994.
- [38]S. Bahuguna, S. Mukhopadhyay, and A. Tiwari, "Sensor-position optimization for flux mapping in a nuclear reactor using compressed sensing," *Ann. Nucl. Energy*, vol. 183, Art. no. 109588, 2023.
- [39]B. Anupreethi *et al.*, "Optimization of flux-mapping in-core detector locations in AHWR using a clustering approach," *Nucl. Eng. Des.*, vol. 366, Art. no. 110756, 2020.
- [40]J.-P. Argaud *et al.*, "Sensor placement in nuclear reactors based on the generalized empirical-interpolation method," *J. Comput. Phys.*, vol. 363, pp. 354–370, 2018.

Appendix A. Derivation of the Mean and Variance of an Exponentially Attenuated Intensity Field

A. 0 Problem statement and notation

- Geometry: A one-dimensional slab of thickness $L > 0$.
- Intensity law: For a mono-energetic, collimated beam the transmitted intensity at depth x is

$$I(x) = I_0 e^{-\mu x}, \quad 0 \leq x \leq L$$

where $I_0 > 0$ is the un-attenuated intensity at the incident surface and $\mu > 0$ is the linear attenuation coefficient (assumed constant over $[0, L]$ after energy grouping).

- Sampling model: Assume the point of interest is selected uniformly at random along the slab,

$$X \sim U(0, L)$$

The intensity random variable is

$$I = I(X) = I_0 e^{-\mu X}$$

Our goal is to derive closed-form expressions for

$$\mathbb{E}[I], \mathbb{E}[I^2], \text{Var}[I] = \mathbb{E}[I^2] - (\mathbb{E}[I])^2$$

Throughout, $\mathbb{E}[\cdot]$ denotes expectation with respect to the uniform density $f_X(x) = 1/L$ on $[0, L]$

A. 1 First moment (mean intensity)

$$\mathbb{E}[I] = \int_0^L I_0 e^{-\mu x} f_X(x) dx = \frac{I_0}{L} \int_0^L e^{-\mu x} dx$$

Use the elementary antiderivative: $\int e^{-\mu x} dx = -\frac{1}{\mu} e^{-\mu x} + C$:

$$\begin{aligned} \frac{I_0}{L} \left[-\frac{1}{\mu} e^{-\mu x} \right]_0^L &= \frac{I_0}{L} \left(-\frac{e^{-\mu L}}{\mu} + \frac{1}{\mu} \right) \\ &= \frac{I_0}{L\mu} (1 - e^{-\mu L}) \end{aligned}$$

Hence

$$\mathbb{E}[I] = \frac{I_0}{\mu L} (1 - e^{-\mu L})$$

A. 2 Second raw moment

$$\mathbb{E}[I^2] = \int_0^L I_0^2 e^{-2\mu x} f_X(x) dx = \frac{I_0^2}{L} \int_0^L e^{-2\mu x} dx.$$

Apply $\int e^{-2\mu x} dx = -\frac{1}{2\mu} e^{-2\mu x} + C$:

$$\frac{I_0^2}{L} \left[-\frac{1}{2\mu} e^{-2\mu x} \right]_0^L = \frac{I_0^2}{L} \left(-\frac{e^{-2\mu L}}{2\mu} + \frac{1}{2\mu} \right) = \frac{I_0^2}{2\mu L} (1 - e^{-2\mu L}).$$

Thus

$$\mathbb{E}[I^2] = \frac{I_0^2}{2\mu L} (1 - e^{-2\mu L}).$$

A. 3 Variance

Substitute (A.1) and (A.2):

$$\begin{aligned} \text{Var}[I] &= \frac{I_0^2}{2\mu L} (1 - e^{-2\mu L}) - \left[\frac{I_0}{\mu L} (1 - e^{-\mu L}) \right]^2 \\ &= I_0^2 \left[\frac{1 - e^{-2\mu L}}{2\mu L} - \frac{(1 - e^{-\mu L})^2}{(\mu L)^2} \right]. \end{aligned}$$

Therefore

$$\text{Var}[I] = I_0^2 \left[\frac{1 - e^{-2\mu L}}{2\mu L} - \frac{(1 - e^{-\mu L})^2}{(\mu L)^2} \right]$$

A. 4 Consistency checks

- Limit $L \rightarrow 0$: $e^{-\mu L} = 1 - \mu L + \frac{1}{2}\mu^2 L^2 + O(L^3)$
Both the bracketed terms in (A.3) behave as $O(L)$, so $\text{Var}[I] \rightarrow 0$ as expected when the sampling window collapses to a single point.
- Limit $\mu L \gg 1$.

With $e^{-\mu L} \approx 0$ and $e^{-2\mu L} \approx 0$,

$$\text{Var } [I] \simeq \frac{I_0^2}{2\mu L},$$

i.e. the variance diminishes inversely with optical thickness because nearly the whole slab lies in a "dark" region of vanishing intensity.